ARCHIVES OF MECHANICS
Arch. Mech. **77** (2), 91–125, 2025, DOI: 10.24423/aom.4617

Analytical and computational methods for a laterally graded surface loaded by a bonded piezoelectric thin film

S. DAG[1)], M. N. BALCI[2)]

[1)] *Department of Mechanical Engineering, Middle East Technical University, Ankara 06800, Turkey, e-mail: sdag@metu.edu.tr (corresponding author)*

[2)] *Department of Mechanical Engineering, Hacettepe University, Ankara 06800, Turkey*

Analytical and computational techniques are developed to carry out stress analyses for an advanced material system comprising a piezoelectric thin film bonded to a laterally graded half-plane. The piezoelectric thin film is assumed to be under electric field loading. Governing partial differential equations are derived in terms of an inhomogeneity parameter in accordance with the theory of elasticity. Applying the Fourier transformation technique and enforcing strain compatibility between the thin film and the laterally graded surface, the problem is reduced to a singular integral equation. A scheme based on the expansion-collocation approach is applied to generate the numerical results. The computational technique is developed by utilizing the finite element method and implemented by means of the general purpose software ANSYS. Comparisons of various stress components indicate a high level of accuracy and reliability in the proposed analytical and computational methods. Parametric analyses illustrate the influences of inhomogeneity, geometry, and elasticity parameters upon interfacial shear stress, thin film normal stress, and lateral normal stress at the bounding surface of the laterally graded medium. In the previous work on thin film loading of functionally graded surfaces, the shear modulus is assumed to be a function of the thickness coordinate. The main novelty in the present study is therefore the development of analytical and computational methods for surfaces possessing the shear modulus variation in the lateral direction. The methods presented could particularly be useful in design, analysis, and optimization studies involving piezoelectric thin films bonded to laterally graded surfaces.

Key words: piezoelectric thin films, laterally graded materials, singular integral equations, finite element analysis, interfacial shear stress.

1. Introduction

Functionally graded materials (FGMs) are advanced composites, which possess spatial variations in the volume fractions of the constituent phases. The variations engender an inhomogeneous macro-structure whose material properties are continuous functions of the physical coordinates. These unique features of FGMs result in additional degrees of freedom in design and can be customized for an improved material response under different types of loading conditions. The main factors associated with this design paradigm are the constituent properties and the variation profiles defining the spatial distributions. Various studies have shown that continuous variations in material properties could particularly be useful in reducing stress concentrations and intensities and suppressing crack initiation and growth in components subjected to high stresses due to mechanical, thermal, electrical, and magnetic effects [1–5]. Among the potential technological use cases of FGMs one can mention thermal barrier, wear-resistant and tribological coatings [6–8], lattice structures [9], bone implants [10], electronic packages [11], and small-scale structures [12, 13]. In recent years, additive manufacturing techniques such as laser synchronous preheating [14], laser metal deposition [15], powder-fed laser directed energy deposition [16], and wire-arc additive manufacturing [17] have significantly contributed to the development and design of different types functionally graded components.

Improved tribological behavior of functionally graded surfaces and coatings gave rise to a large body of work on contact mechanics of inhomogeneous media. Various analytical methods based on integral transform techniques and computational approaches such as the finite element analysis and the boundary element method were proposed to solve problems involving sliding friction [18–20], receding contact [21–23], thermal stresses [24, 25], cracking [26] and moving contact [27, 28]. In all the studies, the loading agent is modelled as a rigid indenter with a given geometry. It was shown that the nature of inhomogeneity may significantly alter the magnitudes of normal contact stress in the contact zone and the lateral normal stress at the surface. Stress intensity factors at the tips of cracks existing in a contact stress field were found to be dependent upon the property distribution profile. The developed methods also allow computation of parameters such as required contact force and sub-surface stresses as functions of material inhomogeneity. The problems are therefore open to optimization and property distributions that minimize contact stress amplitudes and crack driving forces can be identified.

In addition to crack and contact problems, another type of the mixed-boundary value problem that is of particular interest involves thin films bonded to elastic surfaces. Thin films are employed in a wide variety of technological applications such as semiconductor devices [29], solar cells [30], batteries [31], multiferroics [32], cutting tools [33], and piezoelectric energy harvesters and transducers [34, 35]. Stress fields induced by the interaction of a thin film and a functionally graded elastic surface have been examined in a number research articles. Guler [36] developed a singular integral equation based procedure for an elastic thin film bonded to a graded half-plane. Guler *et al.* [37] extended this approach and solved a mixed-boundary value problem involving a thin film and a graded coating. CHEN *et al.* [38] and CHEN *et al.* [39], respectively, examined interfacial behavior of a thin film bonded to an FGM coating/substrate system and a finite thickness graded layer. PEIJIAN *et al.* [40] carried out the interface analysis for a piezoelectric thin film on a graded half-plane. The latest work on thin films also considers the thermoelectric effect [41, 42], thermal loading [43], and material anisotropy [44].

In all articles examining the behavior of a thin film bonded to an FGM surface, the gradation is assumed to be perpendicular to the interface. However, especially with the recent developments in additive manufacturing techniques, it is possible to generate property gradation along the horizontal (lateral) direction at a surface. Gradation in an FGM component along the horizontal or the axial direction is considered within the contexts of several applications including hip prosthesis coatings [45], osseointegrated trans-femoral prostheses [46], and axially graded beams and plates [47, 48]. The change in the direction of gradation results in a different set of governing partial differential equations, for which new procedures are needed for the computation of the required quantities. There is no prior work investigating the response of a system consisting of a thin film and a laterally graded surface. The main objective in the present study is therefore to develop analytical and computational methods for the problem of a piezoelectric thin film bonded to a surface that possesses gradation in the lateral direction.

The problem considered in the analytical formulation comprises an elastic piezoelectric thin film bonded to a laterally graded half-plane. The thin film is subjected to electric field loading in the thickness direction. Governing partial differential equations for the half-plane are obtained by the application of the theory of elasticity, and general solutions are derived by means of the Fourier transformation technique. The formulation is eventually reduced to a singular integral equation by considering the strain compatibility between the piezoelectric thin film and the half-plane. An expansion-collocation technique is developed to numerically solve the singular integral equation. The computational approach is based on the finite element method and integrated into the general purpose analysis software ANSYS. Comparisons of the results generated by the analytical method to those obtained through the finite element analysis verify both approaches. Presented parametric analyses demonstrate the effects of lateral inhomogeneity, thin film location, modulus ratio, and length-to-thickness-ratio of the thin film upon interfacial shear, thin film normal, and lateral normal stress distributions.

The main novel contribution in the present study compared to the state of the art in respective fields is the development of analytical and computational solutions for a piezoelectric thin film bonded to a laterally graded surface. To be able to model the lateral gradation, the shear modulus of the half-plane is assumed to be an exponential function of the lateral direction. However, in all previous articles on thin film problems involving functionally graded materials, the shear modulus is assumed to be a function of the depth coordinate. Dependence of the shear modulus on the lateral coordinate results in a completely different set of governing partial differential equations. Novel analytical and finite element procedures are developed to solve the partial differential equations and to evaluate stresses due to piezoelectric thin film loading. To the best of the authors' knowledge, presented shear and normal stresses as well as thin film stresses are the first results in the literature regarding thin film loading of laterally graded surfaces.

The outline of the paper is as follows: Section 2 describes the analytical solution and provides the details regarding thin film stresses, the singular integral equation, and the numerical scheme; Section 3 introduces the finite element procedures developed to examine the piezoelectric thin film problem; Section 4 presents the verification study and the parametric analyses; and lastly Section 5 concludes the article.

2. Analytical solution

Section 2 consists of three sub-sections. In Section 2.1, we present the modelling approach for the piezoelectric thin film, and derive the expressions for the thin film stress and strain. Section 2.2 outlines the derivation for the laterally graded half-plane and lays out the expressions for the singular integral equation and the lateral normal stress. Section 2.3. details the numerical solution procedure and expounds the details of the expansion-collocation technique.

2.1. Thin film stresses

The geometry of the piezoelectric thin film problem considered is depicted in Fig. 1. A piezoelectric thin film is perfectly bonded to an elastic half-plane, which is graded in y-direction. The problem is defined in the x-y coordinate system attached to the half-plane surface. The interface between the thin film and the half-plane extends from $y = a$ to $y = b$. The composite medium is in the state of either plane stress or strain. Assuming the thin film to be transversely isotropic with poling in x-direction, its constitutive relations are written as follows [49]:

$$\sigma_{xx}^{(\mathrm{f})}(y) = C_{xx}\varepsilon_{xx}^{(\mathrm{f})}(y) + C_{xy}\varepsilon_{yy}^{(\mathrm{f})}(y) - e_{xx}E_x^{(\mathrm{f})}(y), \tag{2.1}$$

$$\sigma_{yy}^{(\mathrm{f})}(y) = C_{xy}\varepsilon_{xx}^{(\mathrm{f})}(y) + C_{yy}\varepsilon_{yy}^{(\mathrm{f})}(y) - e_{yx}E_x^{(\mathrm{f})}(y), \tag{2.2}$$

where the superscript (f) stands for the thin film, $\sigma_{ij}^{(\mathrm{f})}$ are stresses, $\varepsilon_{ij}^{(\mathrm{f})}$ designate strains, C_{ij} are elastic constants, e_{ij} denote piezoelectric constants and $E_x^{(\mathrm{f})}$ is

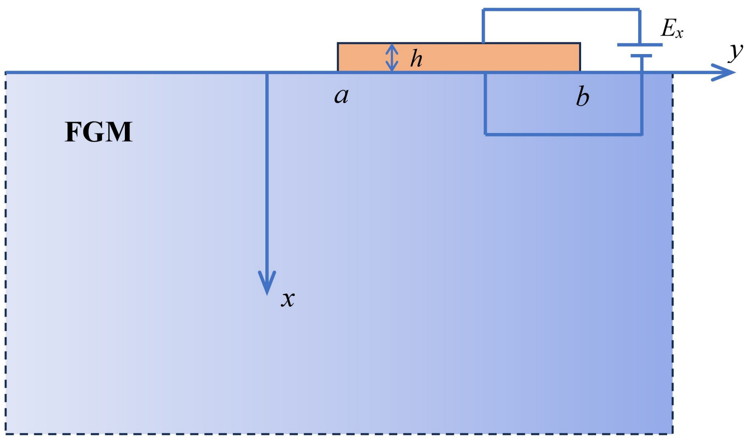

FIG. 1. A piezoelectric thin film bonded to a laterally graded half-plane.

electric field in the x-direction. The normal stress, $\sigma_{xx}^{(\mathrm{f})}$, is zero for the thin film, which leads to

$$\sigma_{yy}^{(\mathrm{f})}(y) = E_f \varepsilon_{yy}^{(\mathrm{f})}(y) - e_f E_x^{(f)}(y), \tag{2.3}$$

$$E_f = \frac{C_{xx}C_{yy} - C_{xy}^2}{C_{xx}}, \qquad e_f = \frac{C_{xx}e_{yx} - C_{xy}e_{xx}}{C_{xx}}. \tag{2.4}$$

The constants E_f and e_f are named as effective Young's modulus and the piezoelectric constant.

Figure 2 shows the free body diagram of the thin film. The loading is due to the electric field, $E_x^{(\mathrm{f})}$. In the modelling of the thin film, membrane stress analysis approximations are utilized. It is assumed that there is no transverse loading on the thin film and that variation of normal stresses throughout the thickness is negligible. Since a thin film is not able to resist bending loads, there is no transverse loading at its top surface and the normal stress, $\sigma_{xx}^{(\mathrm{f})}$, on that plane is zero. This normal stress does not grow to appreciable magnitudes inside the thin film due to the small thickness. As a result, the uniformity assumption in the membrane theoretical framework leads to the conclusion of $\sigma_{xx}^{(\mathrm{f})}$ being zero. The membrane model is implemented in numerous research studies on thin films including those by GULER [36], PEIJIAN *et al.* [40], and DELALE and ERDOGAN [50].

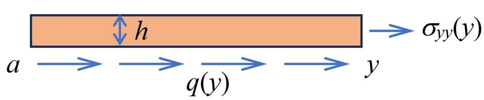

FIG. 2. Free body diagram of the piezoelectric thin film.

The nonzero normal stress, $\sigma_{yy}^{(\mathrm{f})}$, is uniformly distributed across the film thickness; and $q(y)$ in Fig. 2 stands for the shear stress at the interface, $\sigma_{xy}^{(\mathrm{h})}(0,y)$; in which the superscript, (h), designates the half-plane substrate. Equilibrium of the thin film requires that,

$$\sigma_{yy}^{(\mathrm{f})}(y) = -\frac{1}{h}\int_a^y q(y)\,dy. \tag{2.5}$$

Note that in the free body diagram in Fig. 2, the normal stress at the interface, σ_{xx}, is not shown since it is taken as zero. This assumption is required to have a configuration consistent with the membrane approximation, i.e., at no point in the thin film the membrane supports a normal stress in the x-direction; and this includes the interface as well. The thin film is under the effect of shear stress, $q(y)$, as shown in Fig. 2. This shear stress has also a counterpart in the x-direction at the right edge of the thin film. In a detailed fully 2D model, the shear stress at the right edge balances the neglected component, $\sigma_{xx}^{(\mathrm{f})}$. Since this normal stress is zero the shear stress at the right edge is also neglected and not shown in the figure. All of these assumptions are utilized in many previous articles on thin films including [36, 40, 50]. The definition

$$\varepsilon_{yy}^{(\mathrm{f})}(y) = \frac{e_f}{E_f}E_x^{(\mathrm{f})}(y) - \frac{1}{hE_f}\int_a^y q(y)\,dy, \tag{2.6}$$

then follows from Eqs. (2.3) and (2.5).

2.2. Half-plane solution and singular integral equation

The half-plane shown in Fig. 1 is graded in the y-direction, and its elastic properties are expressed as:

$$\mu(y) = \mu_0 \exp(\gamma y), \tag{2.7}$$

$$\kappa = \begin{cases} 3-4\nu & \text{for plane strain,} \\ \dfrac{3-\nu}{1+\nu} & \text{for plane stress,} \end{cases} \tag{2.8}$$

where μ designates shear modulus, κ is Kolosov's constant, and ν denotes Poisson's ratio, which is constant. The shear modulus is represented by an exponential function, and γ is a nonhomogeneity parameter. The constant, μ_0, stands for the value of the shear modulus function at $y=0$. In FGMs, Poisson's ratio varies between values that are relatively close to each other and this variation in general does not impart a notable influence on the mechanical behavior. For this reason, it is considered as a constant in studies involving contact and thin film problems [36]. The constitutive relations are of the forms:

$$\sigma_{xx}^{(\mathrm{h})}(x,y) = \frac{\mu(y)}{\kappa-1}\left\{(\kappa+1)\frac{\partial u^{(\mathrm{h})}}{\partial x} + (3-\kappa)\frac{\partial v^{(\mathrm{h})}}{\partial y}\right\}, \tag{2.9}$$

$$\sigma_{yy}^{(\mathrm{h})}(x,y) = \frac{\mu(y)}{\kappa-1}\left\{(3-\kappa)\frac{\partial u^{(\mathrm{h})}}{\partial x} + (\kappa+1)\frac{\partial v^{(\mathrm{h})}}{\partial y}\right\}, \tag{2.10}$$

$$\sigma_{xy}^{(\mathrm{h})}(x,y) = \mu(x,y)\left\{\frac{\partial u^{(\mathrm{h})}}{\partial y} + \frac{\partial v^{(\mathrm{h})}}{\partial x}\right\}. \tag{2.11}$$

The functions $u^{(\mathrm{h})}$ and $v^{(\mathrm{h})}$ represent displacement components in the x- and y-directions. The governing partial differential equations:

$$\begin{aligned}(\kappa+1)\frac{\partial^2 u^{(\mathrm{h})}}{\partial x^2} + (\kappa-1)\frac{\partial^2 u^{(\mathrm{h})}}{\partial y^2} + 2\frac{\partial^2 v^{(\mathrm{h})}}{\partial x \partial y}& \\ + \gamma(\kappa-1)\frac{\partial u^{(\mathrm{h})}}{\partial y} + \gamma(\kappa-1)\frac{\partial v^{(\mathrm{h})}}{\partial x} &= 0,\end{aligned} \tag{2.12}$$

$$\begin{aligned}(\kappa-1)\frac{\partial^2 v^{(\mathrm{h})}}{\partial x^2} + (\kappa+1)\frac{\partial^2 v^{(\mathrm{h})}}{\partial y^2} + 2\frac{\partial^2 u^{(\mathrm{h})}}{\partial x \partial y}& \\ + \gamma(3-\kappa)\frac{\partial u^{(\mathrm{h})}}{\partial x} + \gamma(\kappa+1)\frac{\partial v^{(\mathrm{h})}}{\partial y} &= 0,\end{aligned} \tag{2.13}$$

are derived by substituting Eqs. (2.7) and (2.9)–(2.11) into the equilibrium equations, $\sigma_{ij,j}^{(\mathrm{h})} = 0$, $i,j = x,y$.

Applying the Fourier transformation in the y-direction to Eqs. (2.12) and (2.13), general solutions for the displacement components are obtained as:

$$u^{(\mathrm{h})}(x,y) = \frac{1}{2\pi}\int_{-\infty}^{\infty}\Big(\sum_{j=1}^{2} C_j \exp(n_j x)\Big)\exp(i\omega y)\, d\omega, \tag{2.14}$$

$$v^{(\mathrm{h})}(x,y) = \frac{1}{2\pi}\int_{-\infty}^{\infty}\Big(\sum_{j=1}^{2} m_j C_j \exp(n_j x)\Big)\exp(i\omega y)\, d\omega, \tag{2.15}$$

$$m_j = \frac{\omega(\omega - i\gamma)(\kappa-1) - n_j^2(\kappa+1)}{\gamma n_j(\kappa-1) + 2i\omega n_j}, \qquad n_j = -\sqrt{t_j},\ j = 1,2, \tag{2.16}$$

$$t_{1,2} = \frac{-z_1 \pm \sqrt{z_1^2 - 4z_2}}{2}, \tag{2.17}$$

$$z_1 = 2i\omega\gamma - 2\omega^2 - \gamma^2\frac{3-\kappa}{\kappa+1}, \qquad z_2 = \omega^2(\omega^2 - 2i\omega\gamma - \gamma^2), \tag{2.18}$$

where ω is the Fourier transform variable, C_j are unknown functions and i is the imaginary unit. The mechanical boundary conditions to be satisfied are:

$$\begin{aligned}\sigma_{xx}^{(\mathrm{h})}(0,y) &= 0, \quad -\infty < y < \infty,\\ \sigma_{xy}^{(\mathrm{h})}(0,y) &= \begin{cases} q(y), & a < y < b,\\ 0, & y < a,\ y > b.\end{cases}\end{aligned} \tag{2.19}$$

$$\varepsilon_{yy}^{(\mathrm{f})} = \varepsilon_{yy}^{(\mathrm{h})}(0,y), \quad -\infty < y < \infty. \tag{2.20}$$

Additionally, all field variables must conform to the regularity condition, which requires boundedness of the field variables as $\sqrt{x^2+y^2} \to \infty$. Using the constitutive relations and the boundary conditions, the unknown functions are found as follows:

$$C_j(\omega) = \frac{E_j(\omega)}{\mu_0} \int_a^b q_1(t)\exp(-i\omega t)\,dt, \qquad j = 1,2, \tag{2.21}$$

$$q_1(t) = q(t)\exp(-\gamma t). \tag{2.22}$$

The linear system,

$$\sum_{j=1}^{2} (n_j(\kappa+1) + i\omega m_j(3-\kappa))E_j = 0, \tag{2.23}$$

$$\sum_{j=1}^{2} (i\omega + m_j n_j)E_j = 1, \tag{2.24}$$

yields the functions, $E_j(\omega)$.

The singular integral equation is to be derived by equating the normal strain, $\varepsilon_{yy}^{(\mathrm{h})}(0,y)$, to that obtained for the thin film. After a lengthy procedure involving asymptotic analyses of the pertaining integrands, the normal strain at the surface of the half-plane is derived in the following form:

$$\begin{aligned}\varepsilon_{yy}^{(\mathrm{h})}(0,y) = \frac{1}{2\pi\mu_0}\int_a^b \bigg\{ &\frac{d_0}{y-t} - c_1\,\mathrm{Ci}(A_1|y-t|)\\ &+ h_1(y,t) + h_2(y,t)\bigg\} q_1(t)\,dt, \qquad -\infty < y < \infty,\end{aligned} \tag{2.25}$$

$$h_1(y,t) = \int_0^{A_1} K_1(\omega)\cos(\omega(y-t))\,d\omega \tag{2.26}$$

$$+ \int_{A_1}^{\infty} \left(K_1(\omega) - \frac{c_1}{\omega} - \frac{c_3}{\omega^3} - \frac{c_5}{\omega^5}\right)\cos(\omega(y-t))\,d\omega$$

$$+ \int_{A_1}^{\infty} \left(\frac{c_3}{\omega^3} + \frac{c_5}{\omega^5}\right)\cos(\omega(y-t))d\omega,$$

$$h_2(y,t) = \int_0^{A_2} (K_2(\omega) - d_0)\sin(\omega(y-t))\,d\omega \tag{2.27}$$

$$+ \int_{A_2}^{\infty} (K_2(\omega) - d_0 - \frac{d_2}{\omega^2} - \frac{d_4}{\omega^4})\sin(\omega(y-t))\,d\omega$$

$$+ \int_{A_1}^{\infty} \left(\frac{d_2}{\omega^2} + \frac{d_4}{\omega^4}\right)\sin(\omega(y-t))\,d\omega,$$

$$K_1(\omega) = \Phi(\omega) + \Phi(-\omega), \qquad K_2(\omega) = i(\Phi(\omega) - \Phi(-\omega)), \tag{2.28}$$

$$\Phi(\omega) = i\omega\sum_{j=1}^{2} m_j E_j, \tag{2.29}$$

where Ci in Eq. (2.25) is the cosine integral. A_1 and A_2 are integration cut-off points; and c_i and d_i are determined through asymptotic analyses. The coefficients are given as:

$$d_0 = \frac{\kappa+1}{2}, \qquad c_1 = \frac{(\kappa+1)\gamma}{4}, \tag{2.30}$$

$$d_2 = -\frac{\kappa\gamma^2}{4}, \qquad c_3 = \frac{(1-2\kappa)\gamma^3}{8}, \tag{2.31}$$

$$d_4 = \frac{(4\kappa^2+\kappa-4)\gamma^4}{16(\kappa+1)}, \qquad c_5 = \frac{(8\kappa^2+\kappa-12)\gamma^5}{32(\kappa+1)}. \tag{2.32}$$

The singular integral equation

$$\frac{1}{2\pi\mu_0}\int_a^b \left\{\frac{d_0}{y-t} - c_1\,\mathrm{Ci}(A_1|y-t|) + h_1(y,t) + h_2(y,t)\right\} q_1(t)\,dt \tag{2.33}$$

$$+ \frac{1}{E_f h}\int_a^y \exp(\gamma t) q_1(t)\,dt = \frac{e_f}{E_f} E_x^{(\mathrm{f})}, \quad a < y < b,$$

is obtained by equating the half plane normal strain, $\varepsilon_{yy}^{(\mathrm{h})}(0,y)$, given by Eq. (2.25) to the thin film strain expressed by Eq. (2.6).

Note that the half-plane problem tackled involves mechanical boundary conditions but no electrical conditions. This is due to the fact that the half-plane does not possess piezoelectric properties. The mechanical boundary conditions are imposed by Eqs. (2.19) and (2.20). Influence of piezoelectricity is included through the constitutive relation of the thin film, which is expressed by Eq. (2.1).

In addition to the singular integral equation, the equilibrium condition of the piezoelectric thin film

$$\int_a^b \exp(\gamma t) q_1(t)\, dt = 0, \tag{2.34}$$

is also required in the solution. This condition follows from Eq. (2.5). The unknown shear stress at the interface of the thin film and the half-plane; and the normal stress in the thin film can be computed once Eqs. (2.33) and (2.34) are solved simultaneously.

Another important variable of interest that affects the failure of a laterally graded half-plane is the normal stress at $x = 0$, i.e., $\sigma_{yy}^{(\mathrm{h})}(0,y)$. This stress component is derived by utilizing Eq. (2.10) and applying asymptotic analyses on the integrands of the related kernels. The expression is of the form:

$$\sigma_{yy}^{(\mathrm{h})}(0,y) = \frac{\mu(y)}{\kappa-1}\left\{(\kappa+1)\varepsilon_{yy}^{(\mathrm{h})}(0,y) + (3-\kappa)\frac{\partial u^{(\mathrm{h})}(0,y)}{\partial y}\right\}, \tag{2.35}$$

where the normal strain at the surface, $\varepsilon_{yy}^{(\mathrm{h})}(0,y)$, is given by Eq. (2.25), and the normal strain in the x-direction is derived as:

$$\begin{aligned}\frac{\partial u^{(\mathrm{h})}(0,y)}{\partial x} = \frac{1}{2\pi\mu_0}\int_a^b \bigg\{ & \frac{g_0}{y-t} - f_1 \operatorname{Ci}(A_3|y-t|) \\ & + p_1(y,t) + p_2(y,t)\bigg\} q_1(t)\, dt, \quad -\infty < y < \infty,\end{aligned} \tag{2.36}$$

$$\begin{aligned}p_1(y,t) = {} & \int_0^{A_3} L_1(\omega)\cos(\omega(y-t))\, d\omega \\ & + \int_{A_3}^{\infty}\left(L_1(\omega) - \frac{f_1}{\omega} - \frac{f_3}{\omega^3}\right)\cos(\omega(y-t))\, d\omega + \int_{A_3}^{\infty}\frac{f_3}{\omega^3}\, d\omega,\end{aligned} \tag{2.37}$$

$$p_2(y,t) = \int_0^{A_4} \{L_2(\omega) - g_0\} \sin(\omega(y-t))\, d\omega \tag{2.38}$$
$$+ \int_{A_4}^{\infty} \left(L_2(\omega) - g_0 - \frac{g_2}{\omega^2} - \frac{g_4}{\omega^4}\right) \sin(\omega(y-t))\, d\omega$$
$$+ \int_{A_4}^{\infty} \left\{\frac{g_2}{\omega^2} + \frac{g_4}{\omega^4}\right\} \sin(\omega(y-t))\, d\omega,$$

$$L_1(\omega) = \Gamma(\omega) + \Gamma(-\omega), \qquad L_2(\omega) = i(\Gamma(\omega) - \Gamma(-\omega)), \tag{2.39}$$

$$\Gamma(\omega) = \sum_{j=1}^{2} n_j E_j, \tag{2.40}$$

$$g_0 = \frac{\kappa - 3}{2}, \qquad f_1 = \frac{(\kappa-3)\gamma}{4}, \tag{2.41}$$

$$g_2 = \frac{\kappa(\kappa-3)\gamma^2}{4(\kappa+1)}, \qquad f_3 = \frac{(1-2\kappa)(\kappa-3)\gamma^3}{8(\kappa+1)}, \tag{2.42}$$

$$g_4 = \frac{(4\kappa^2 + \kappa - 4)(\kappa-3)\gamma^4}{16(\kappa+1)^2}. \tag{2.43}$$

The constants, A_3 and A_4, are integration cut-off points; and g_i and f_i are the coefficients that are extracted by means of asymptotic analyses.

2.3. Numerical solution

In order to express the integral equation in terms of dimensionless variables and constants, we introduce the following definitions:

$$y = \frac{b-a}{2}s + \frac{b+a}{2}, \qquad t = \frac{b-a}{2}r + \frac{b+a}{2}, \tag{2.44}$$

$$q_{1n}(r) = \frac{q_1\left(\frac{b-a}{2}r + \frac{b+a}{2}\right)}{\mu_0\left(\frac{e_f}{E_f} E_x^{(\mathrm{f})}\right)}, \tag{2.45}$$

$$\gamma_1 = \frac{b-a}{2}\gamma, \qquad \gamma_2 = \frac{b+a}{2}\gamma, \qquad \bar{c}_1 = \frac{\kappa+1}{4}\gamma_1, \qquad \bar{A}_1 = \frac{b-a}{2}A_1, \tag{2.46}$$

$$\bar{h}_i(s,r) = \frac{b-a}{2} h_i\left(\frac{b-a}{2}s + \frac{b+a}{2}, \frac{b-a}{2}r + \frac{b+a}{2}\right), \qquad i = 1,2. \tag{2.47}$$

The singular integral equation and the equilibrium condition for the piezoelectric thin film are then written as follows:

$$\frac{1}{2\pi}\int_{-1}^{1}\left\{\frac{d_0}{s-r}-\bar{c}_1\,\mathrm{Ci}(\bar{A}_1|s-r|)+\bar{h}_1(s,r)+\bar{h}_2(s,r)\right\}q_{1n}(r)\,dr + \frac{(b-a)\mu_0}{2E_f h}\int_{-1}^{s}\exp(\gamma_1 r+\gamma_2)q_{1n}(r)\,dr = 1, \quad -1<s<1, \tag{2.48}$$

$$\int_{-1}^{1}\exp(\gamma_1 r+\gamma_2)q_{1n}(r)\,dr = 0. \tag{2.49}$$

The unknown of the equation system is $q_{1n}(r)$. The Cauchy singularity indicates that it can be expanded into a series of the form

$$q_{1n}(r)=\frac{1}{\sqrt{1-r^2}}\sum_{n=0}^{\infty}B_nT_n(r), \tag{2.50}$$

where the square-root singularity at the ends is quantified by the term, $1/\sqrt{1-r^2}$, B_n's are unknown coefficients, and $T_n(r)$ is the Chebyshev polynomial of the first kind of the order n.

Substituting Eq. (2.50) into Eqs. (2.48) and (2.49) and using the properties of the Chebyshev polynomials [51], the functional equation system

$$\frac{d_0}{2}\sum_{n=1}^{\infty}B_nU_{n-1}(s)-\sum_{n=0}^{\infty}B_n(k_{11n}(s) + k_{12n}(s)+k_{13n}(s)) = -1, \quad -1<s<1, \tag{2.51}$$

$$\sum_{n=0}^{\infty}B_nk_{2n}=0, \tag{2.52}$$

is obtained. $U_n(s)$ here is the Chebyshev polynomial of the second kind of the order n, and

$$k_{11n}(s) = -\frac{\bar{c}_1}{2\pi}\int_{-1}^{1}\mathrm{Ci}(\bar{A}_1|s-r|)\frac{T_n(r)}{\sqrt{1-r^2}}\,dr, \tag{2.53}$$

$$k_{12n}(s) = \frac{1}{2\pi}\int_{-1}^{1}(\bar{h}_1(s,r)+\bar{h}_2(s,r))\frac{T_n(r)}{\sqrt{1-r^2}}\,dr, \tag{2.54}$$

$$k_{13n}(s) = \frac{\mu_0(b-a)}{2E_f h}\int_{-1}^{s}\exp(\gamma_1 r+\gamma_2)\frac{T_n(r)}{\sqrt{1-r^2}}\,dr, \tag{2.55}$$

$$k_{2n} = \int_{-1}^{1}\exp(\gamma_1 r+\gamma_2)\frac{T_n(r)}{\sqrt{1-r^2}}\,dr. \tag{2.56}$$

Equation (2.51) is approximated by truncating the infinite series at $n = N$, and using the collocation points,

$$s_i = \cos\left(\frac{\pi(2i-1)}{2N}\right), \qquad i = 1, \ldots, N. \tag{2.57}$$

Then, an $(N+1)\times(N+1)$ linear system is generated by considering Eqs. (2.51) and (2.52), the solution of which yields the unknown coefficients, B_n. The shear stress at the thin film – half-plane interface and the normal stress in the piezoelectric thin film are computed by

$$S_{xy}(s) = \frac{\sigma_{xy}^{(\mathrm{h})}\left(0, \frac{b-a}{2}s + \frac{b+a}{2}\right)}{\mu_0 \frac{e_f}{E_f} E_x^{(\mathrm{f})}} = \frac{\exp(\gamma_1 s + \gamma_2)}{\sqrt{1-s^2}} \sum_{n=0}^{N} B_n T_n(s), \tag{2.58}$$

$$S_{yy}(s) = \frac{\sigma_{yy}^{(\mathrm{f})}\left(\frac{b-a}{2}s + \frac{b+a}{2}\right)}{\mu_0 \frac{e_f}{E_f} E_x^{(\mathrm{f})}} = -\sum_{n=0}^{N} B_n k_{13n}(s). \tag{2.59}$$

The normal stress in the y-direction at $x = 0$ in the half-plane is defined by Eqs. (2.35) and (2.36) and its dimensionless form is expressed as follows:

$$\begin{aligned}\Omega_{yy}(s) &= \frac{\sigma_{yy}^{(\mathrm{h})}\left(0, \frac{b-a}{2}s+\frac{b+a}{2}\right)}{\mu_0 \frac{e_f}{E_f} E_x^{(\mathrm{f})}} \\ &= \frac{\exp(\gamma_1 s+\gamma_2)}{\kappa-1}\left\{\sum_{n=0}^{N} B_n(M_{1n}(s)+M_{2n}(s)+M_{3n}(s))\right\}, \qquad -\infty < s < \infty,\end{aligned} \tag{2.60}$$

$$M_{1n}(s) = \begin{cases} -\frac{(\kappa+1)d_0+(3-\kappa)g_0}{2} U_{n-1}(s), & |s| < 1,\ n > 0, \\ 0, & |s| < 1,\ n = 0, \\ -\frac{(\kappa+1)d_0+(3-\kappa)g_0}{2} \frac{(\sqrt{s^2-1}-|s|)^n}{(-s/|s|)^{n+1}\sqrt{s^2-1}}, & |s| > 1,\ n \geqslant 0, \end{cases} \tag{2.61}$$

$$M_{2n}(s) = -\frac{1}{2\pi}\int_{-1}^{1} \frac{(\kappa+1)\bar{c}_1 \operatorname{Ci}(\bar{A}_1|s-r|)+(3-\kappa)\bar{f}_1 \operatorname{Ci}(\bar{A}_3|s-r|)}{(s-r)\sqrt{1-r^2}} T_n(r)\, dr, \tag{2.62}$$

$$M_{3n}(s) = \frac{1}{2\pi}\int_{-1}^{1} \frac{(\kappa+1)(\bar{h}_1(s,r)+\bar{h}_2(s,r))+(3-\kappa)(\bar{p}_1(s,r)+\bar{p}_2(s,r))}{(s-r)\sqrt{1-r^2}} T_n(r)\, dr, \tag{2.63}$$

$$\bar{f}_1 = \frac{\kappa-3}{4}\gamma_1, \qquad \bar{A}_3 = \frac{b-a}{2}A_3, \tag{2.64}$$

$$\bar{p}_i(s,r) = \frac{b-a}{2} p_i\left(\frac{b-a}{2}s+\frac{b+a}{2}, \frac{b-a}{2}r+\frac{b+a}{2}\right), \qquad i = 1, 2. \tag{2.65}$$

Another quantity of interest in problems involving stress singularities is the stress intensity factor (SIF). For the thin film problem considered, mode II stress intensity factors at the end points of the interface are defined as follows:

$$K_{II}(a) = \lim_{y\to a^+} \sqrt{2(y-a)}\sigma_{xy}^{(\mathrm{h})}(0,y), \tag{2.66}$$

$$K_{II}(b) = \lim_{y\to b^-} \sqrt{2(b-y)}\sigma_{xy}^{(\mathrm{h})}(0,y). \tag{2.67}$$

By utilizing the definition given by Eq. (2.50), dimensionless SIFs are derived in the form:

$$K_{IIn}(a) = \frac{K_{II}(a)}{\sqrt{b-a}\mu_0 \frac{e_f}{E_f} E_x^{(\mathrm{f})}} = \frac{\exp(\gamma_2-\gamma_1)}{\sqrt{2}} \sum_{n=0}^{\infty} B_n T_n(-1), \tag{2.68}$$

$$K_{IIn}(b) = \frac{K_{II}(b)}{\sqrt{b-a}\mu_0 \frac{e_f}{E_f} E_x^{(\mathrm{f})}} = \frac{\exp(\gamma_2-\gamma_1)}{\sqrt{2}} \sum_{n=0}^{\infty} B_n T_n(1). \tag{2.69}$$

3. Finite element analysis

In addition to the analytical technique described in Section 2, the defined problem is examined by means of the finite element method. In this section, we provide the details regarding the finite element approach such as the element types, number of elements, interface and boundary conditions, and treatment of gradation.

The developed computational procedure is integrated into the general purpose finite element analysis software ANSYS. Figure 3 depicts the constructed finite element model, which comprises the piezoelectric thin film and the laterally graded half-plane. The FEA mesh contains a total of 198110 triangular finite elements. 144858 of these elements are used for the laterally graded half-plane, and 53252 elements are employed for the discretization of the thin film. The triangular finite element is generated by merging the three nodes of an 8-noded quadrilateral finite element. The 8-noded quadrilateral element is named as PLANE223 in ANSYS library. The quadrilateral element, its degenerate triangular form, and the element in the isoparametric coordinate system are shown in Fig. 4.

Displacement components in two orthogonal directions and the electric potential are the three degrees of freedom at each node of the quadrilateral element. This element allows modelling of piezoelectric, piezoresistive, and thermoelectric materials; and can be used in multi-physics simulations involving structural-thermal or structural-electrical effects. In this study, the piezoelectric option is considered to simulate the structural response due to the applied electric

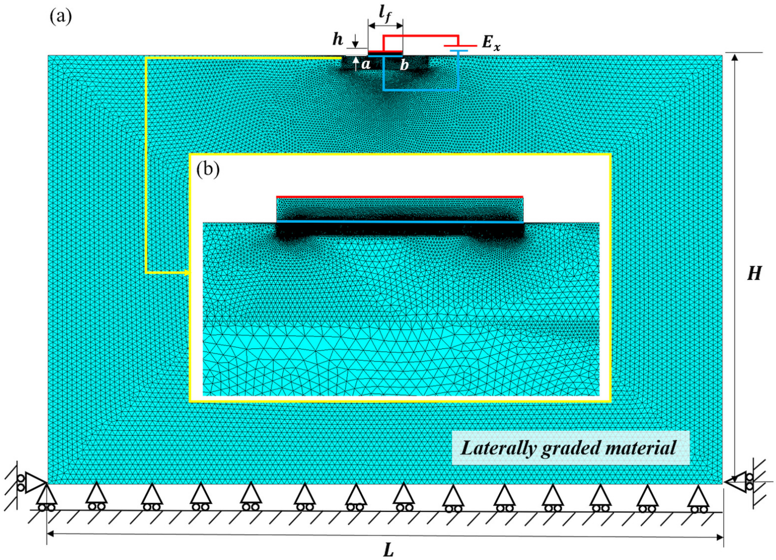

FIG. 3. (a) Entire finite element mesh; (b) close-up view of the thin film and the interface.

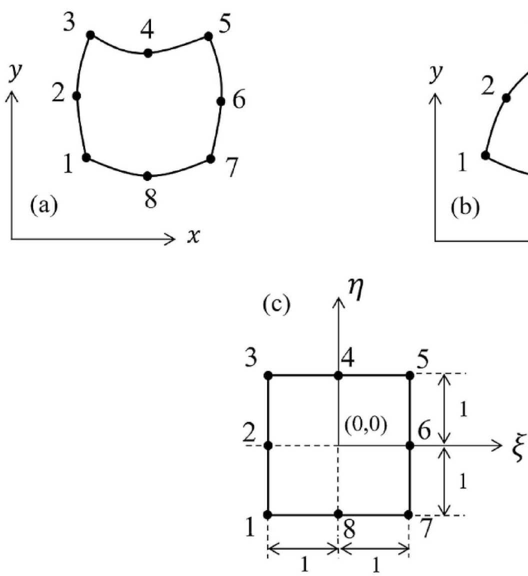

FIG. 4. (a) Quadrilateral finite element; (b) triangular form; (c) element in the isoparametric coordinate system.

potential. The triangular form of the element is employed in the construction of the meshes of both the piezoelectric thin film and the laterally graded substrate. However, the piezoelectric properties of the laterally graded medium are set as zero since the half-plane displays solely linear elastic mechanical behavior. The interpolation for each of the displacement components, and the electric potential in the isoparametric coordinate system is expressed as follows:

$$\phi(\xi,\eta)=\sum_{i=1}^{8}N_i(\xi,\eta)\varphi_i, \tag{3.1}$$

where φ represents a displacement component or the electric potential and the shape functions are given by [52]:

$$N_1(\xi,\eta)=\frac{1}{4}(1-\xi)(1-\eta)(-\xi-\eta-1),\quad N_2(\xi,\eta)=\frac{1}{4}(1-\xi)(1-\eta^2), \tag{3.2}$$

$$N_3(\xi,\eta)=\frac{1}{4}(1-\xi)(1+\eta)(-\xi+\eta-1),\quad N_4(\xi,\eta)=\frac{1}{2}(1-\xi^2)(1+\eta), \tag{3.3}$$

$$N_5(\xi,\eta)=\frac{1}{4}(1+\xi)(1+\eta)(\xi+\eta-1),\quad N_6(\xi,\eta)=\frac{1}{2}(1+\xi)(1-\eta^2), \tag{3.4}$$

$$N_7(\xi,\eta)=\frac{1}{4}(1+\xi)(1-\eta)(\xi-\eta-1),\quad N_8(\xi,\eta)=\frac{1}{2}(1-\xi^2)(1-\eta). \tag{3.5}$$

As depicted in Fig. 3, the dimensions of the laterally graded half-plane are symbolized by H and L, whereas l_f and h designate the length and the thickness of the thin film, respectively. The dimensions H and L are assigned sufficiently large values to be able to simulate the conditions for the half-plane, whose mathematical definition does not involve remote boundaries. The particular ratios considered in the implementation are $L/l_f = 20$ and $H/l_f = 12.5$. In FEA modeling, the piezoelectric thin film is assumed to be perfectly bonded to the laterally graded surface. This implies continuity of the displacements as follows:

$$u^{(\mathrm{f})}(y)=u^{(\mathrm{h})}(0,y),\qquad v^{(\mathrm{f})}(y)=v^{(\mathrm{h})}(0,y). \tag{3.6}$$

The interface between the thin film and the half-plane contains a total of 6808 nodes. The mesh density is significantly refined at the end points of the interface to be able accurately capture the singularities and stress variations. Note that, the shear stress at the interface and the lateral normal stress at the surface of the half-plane both possess singularities at the ends and a sufficient level of refinement at these points is imperative for an accurate analysis.

The electrical and structural boundary conditions imposed in the analyses are also depicted in Fig. 3. The red line at the top surface of the piezoelectric thin film indicates the surface on which an electric potential, V_x, is applied. This surface acts as the positive electrode. The blue line at the bottom surface stands for the electrical ground surface on which the voltage is specified as zero. This surface can be considered as the negative electrode. Electric potential values are identical on the nodes of each surface and there is a unique voltage drop across the thickness of the thin film. The bottom surface of the half-plane is constrained in the vertical direction. The node at the lower left corner is fixed to prevent rigid body motion.

An important consideration in the finite element analysis of FGMs is the incorporation of smooth spatial variations of the physical properties into the model. There are primarily two approaches of considering the spatial variations of elastic properties. The first method is known as the graded finite element approach, which entails computation of all required properties at each Gauss point of a finite element during the formation of the element stiffness matrix. The second technique – named as the homogeneous finite element procedure – involves calculation of all properties at the centroid of each finite element. Previous studies [53, 54] prove that both methods lead to computational results of high accuracy, provided that a sufficient level of mesh refinement is present in the model. In the current study, the homogeneous finite element approach is adopted so as to account for the smooth spatial variations in the elastic properties of the laterally graded medium.

4. Numerical results

Section 4 is organized in 3 subsections. In Section 4.1, we present a verification study, which involves comparisons of analytical and computational results. Section 4.2 reports a second validation achieved by a comparison of our results to those available in the literature for a limiting case. Section 4.3 includes parametric analyses, which demonstrate the influences of the problem parameters on stress distributions and stress intensity factors.

4.1. Verification

A detailed verification study is carried out by comparing the numerical results evaluated by means of the singular integral equation technique to those generated by the finite element method. The first set of comparisons given in Fig. 5 involves, the dimensionless interface shear stress, $S_{xy}(s)$, whose expression is provided by Eq. (2.58). The dimensionless coordinate, s, is defined by Eq. (2.44). The comparisons are provided for 5 different values of the dimensionless inhomogeneity parameter, $\gamma(b-a)$. The thin film is symmetrically located with respect to origin, i.e., $b=-a$. In all cases, analytical results are in excellent agreement with those obtained by the finite element method. Note that the load-

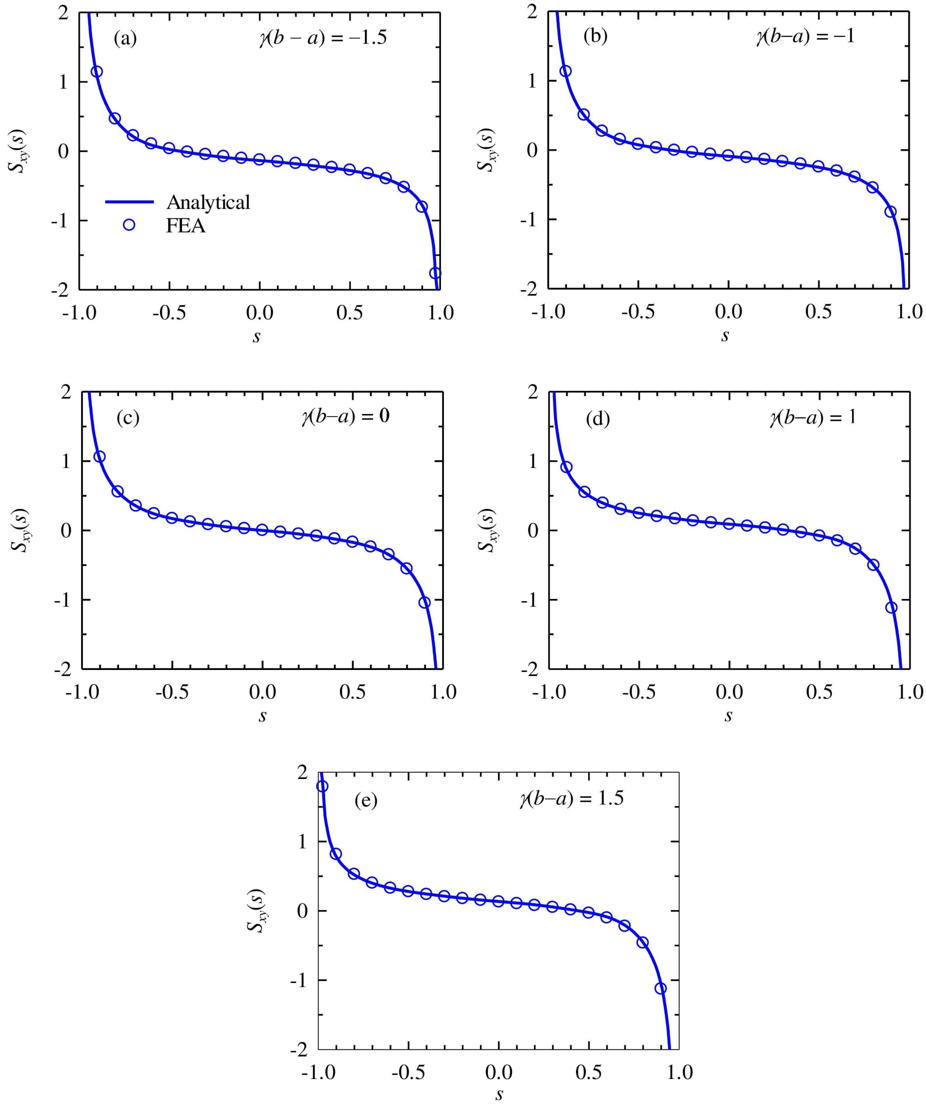

Fig. 5. Comparisons of dimensionless shear stress, $S_{xy}(s)$: (a) $\gamma(b-a) = -1.5$; (b) $\gamma(b-a) = -1$; (c) $\gamma(b-a) = 0$; (d) $\gamma(b-a) = 1$; (e) $\gamma(b-a) = 1.5$; $b = -a$, $\mu_0/E_f = 0.3$, $(b-a)/h = 10$, $v = 0.25$.

ing is due to the electric field, $E_x^{(\mathrm{f})}$, which is present as a normalization factor in Eq. (2.58). Shear stress transitions from positive to negative as the normalized position, s, is increased from -1 to 1. At both ends of the interface, $s = \pm 1$, shear stress possesses the square-root singularity. The shear stress is perfectly anti-symmetric with respect to the axis, $s = 0$, when the half-plane is homoge-

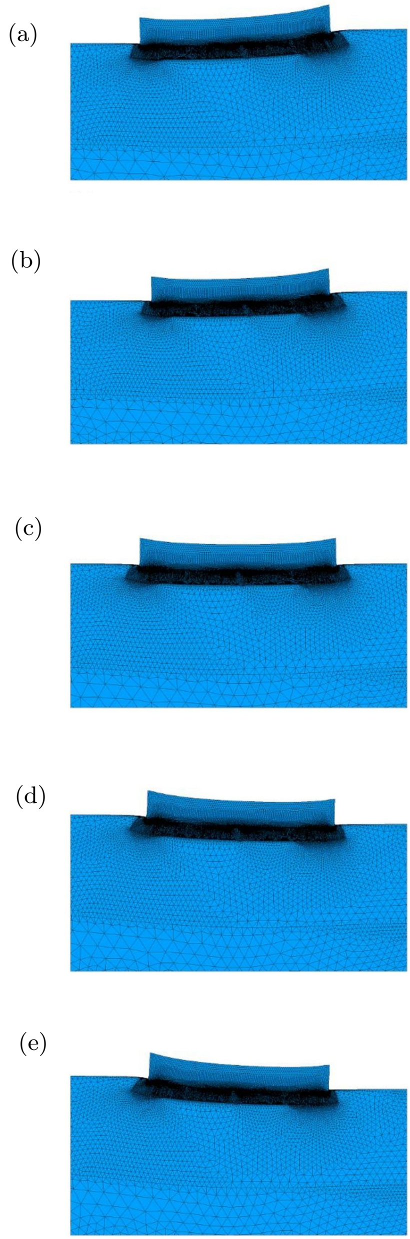

Fig. 6. Deformed shapes: (a) $\gamma(b-a) = -1.5$; (b) $\gamma(b-a) = -1$; (c) $\gamma(b-a) = 0$; (d) $\gamma(b-a) = 1$; (e) $\gamma(b-a) = 1.5$; $b = -a$, $\mu_0/E_f = 0.3$, $(b-a)/h = 10$, $\upsilon = 0.25$.

neous, i.e., when $\gamma(b-a) = 0$. However, this anti-symmetry is distorted when $\gamma(b-a)$ becomes nonzero. Close-up views of the deformed finite element model displaying the thin film and its proximity are provided in Fig. 6.

A second set of comparisons is generated by considering the dimensionless normal stress in the thin film, $S_{yy}(s)$, whose definition is expressed by Eq. (2.59). The findings are provided in Fig. 7. The computations are again carried out for five different values of $\gamma(b-a)$, and the analytical results are found to be in perfect agreement with those obtained by the finite element method. In finite element analyses, the normal stress is computed at the bottom surface of the thin

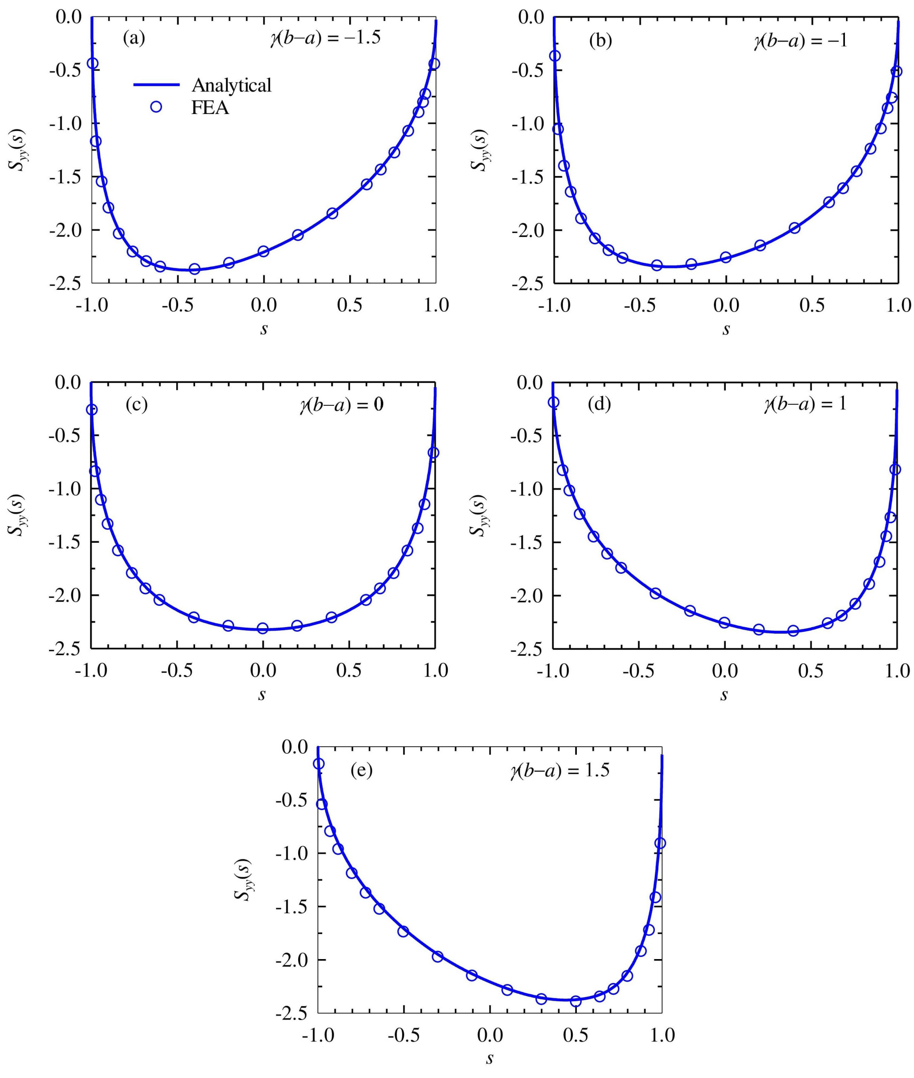

Fig. 7. Comparisons of dimensionless thin-film stress, $S_{yy}(s)$: (a) $\gamma(b-a)=-1.5$; (b) $\gamma(b-a)=-1$; (c) $\gamma(b-a)=0$; (d) $\gamma(b-a)=1$; (e) $\gamma(b-a)=1.5$; $b=-a$, $\mu_0/E_f=0.3$, $(b-a)/h=10$, $v=0.25$.

film. As expected, the normal stress is zero at the stress-free ends, $s = \pm 1$. It goes through a minimum within the thin film; and is symmetric with respect to $s = 0$ for $\gamma(b-a) = 0$. The curves are tilted towards $s = -1$ for negative values of $\gamma(b-a)$ and towards $s = 1$ for positive values. Comparisons of the dimensionless lateral normal stress, $\Omega_{yy}(s)$, which is computed at the surface of the graded medium, are provided in Fig. 8. The expression of the normal stress is given by

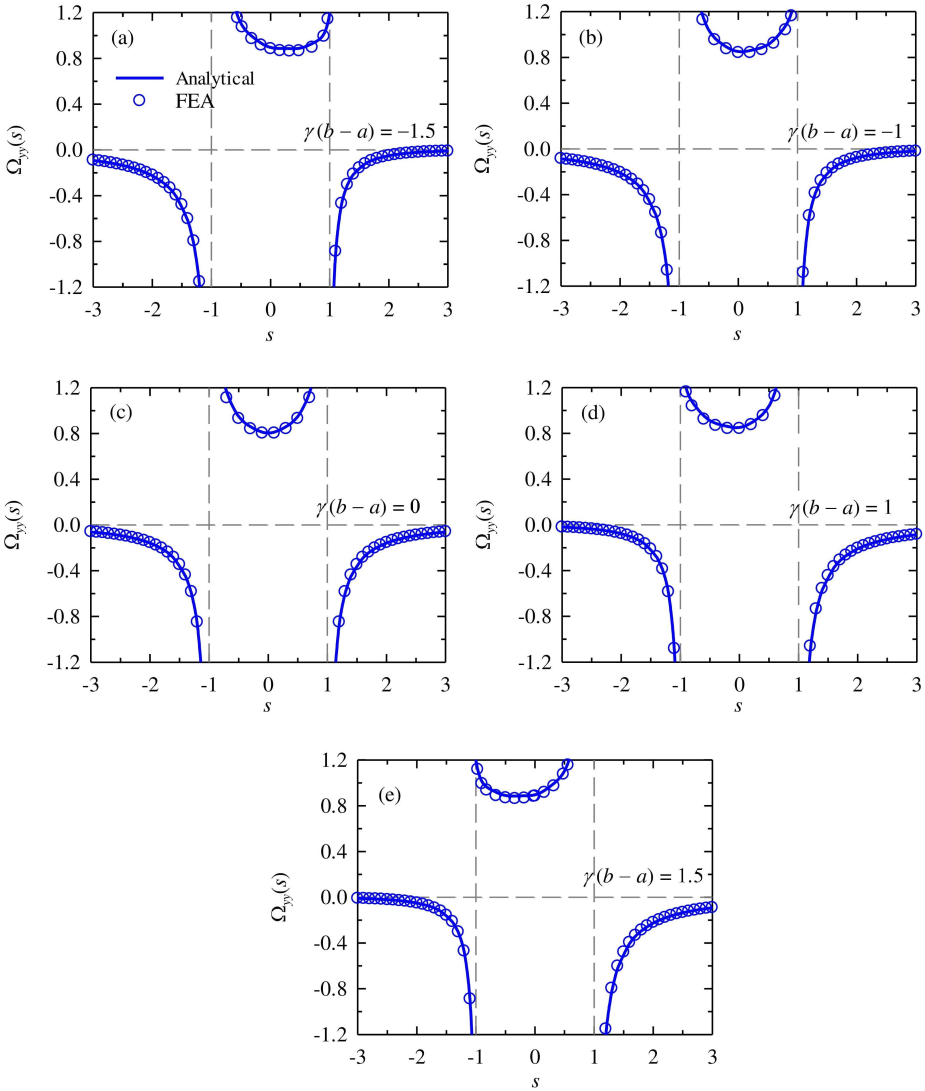

FIG. 8. Comparisons of dimensionless lateral stress, $\Omega_{yy}(s)$: (a) $\gamma(b-a) = -1.5$; (b) $\gamma(b-a) = -1$; (c) $\gamma(b-a) = 0$; (d) $\gamma(b-a) = 1$; (e) $\gamma(b-a) = 1.5$; $b = -a$, $\mu_0/E_f = 0.3$, $(b-a)/h = 10$, $v = 0.25$.

Eqs. (2.60)–(2.65). The analytical results are in excellent agreement with those calculated by FEA for all $\gamma(b-a)$ values considered. The lateral normal stress is of particular significance since a high positive value at a certain location points to the possibility of crack initiation and growth. It is seen that under the given electric field loading, the lateral normal stress is always positive at the interface between the thin film and the half-plane ($|s| < 1$). The positive singularities at the ends of the interface zone point out to the probability of fracture failure at those points. Outside of the interfacial zone ($|s| > 1$), the lateral normal stress is always compressive, and its amplitude tends to $-\infty$ as $s \to -1^-$ and $s \to 1^+$. The lateral stress also satisfies the regularity condition, i.e., it approaches zero as $s \to \pm\infty$.

4.2. Analysis of a limiting case

The previous section presents comparisons between our analytical and computational results, and the high level of agreement is a testament to the high level of accuracy achieved by both methods. A second verification study is conducted by comparing our analytical results to those provided by PEIJIAN *et al.* [40] for a limiting case. The problem tackled by PEIJIAN *et al.* [40] consists of a piezoelectric thin film bonded to a homogeneous half-plane. The thin film is assumed to be under uniform electric field loading. The geometry is therefore exactly the same as the geometry depicted in Fig. 1. However, there is no gradation and the shear modulus and Poisson's ratio take on constant values.

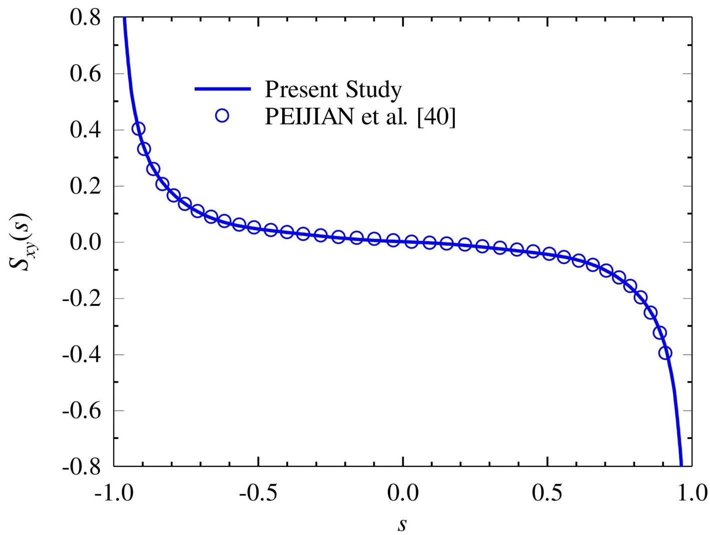

FIG. 9. Comparisons of the analytical results to those given by PEIJIAN *et al.* [40]; $\gamma(b-a) = 0$, $\gamma(b+a) = 0$, $\nu = 0.3$, $(b-a)/h = 10$, $\mu_0/E_f = 2.28(1-\nu)/\pi$.

The numerical results pertaining to the homogeneous half-plane model can be generated via our analytical methodology by specifying the inhomogeneity constant $\gamma(b-a)$ as zero. In such a case, the parameter $\gamma(b+a)$ does not impact the outcome since for a homogeneous half-plane, the thin film problem is self-similar, i.e., the location of the thin film does not influence the stress distribution.

Figure 9 presents comparisons of our numerical results for the dimensionless shear stress at the interface, $S_{xy}(s)$, to those provided by PEIJIAN *et al.* [40]. Length-to-thickness and modulus ratios, $(b-a)/h$ and μ_0/E_f, are respectively taken as 10 and $2.28(1-\nu)/\pi$. Our analytical results are seen to be in excellent agreement with those given by PEIJIAN *et al.* [40]. Hence, these findings are deemed to be another independent verification of the developed analytical technique.

4.3. Parametric analyses

In this section, we present the results of the analytical and computational studies carried out to examine the influences of problem parameters on the stress distributions and stress intensity factors. Analytical results involving the interface shear stress, $S_{xy}(s)$, and the thin film normal stress, $S_{yy}(s)$, are presented in Figs. 10–13. SIFs are tabulated in Tables 1–4. Figure 10 illustrates the effect of the inhomogeneity parameter, $\gamma(b-a)$, on $S_{xy}(s)$, and $S_{yy}(s)$, for $b=-a/2$. Figure 10(a) shows that, as $\gamma(b-a)$ is increased from -1.5 to 1.5, there tends to be an increase in the dimensionless shear stress, $S_{xy}(s)$, within the inner section of the interfacial zone. The stress becomes square-root singular as s approaches the end points -1 and 1. The impact on $S_{yy}(s)$ is depicted in Fig. 10(b). The normal stress attains a minimum value and is symmetric with respect to $s=0$ when $\gamma(b-a)=0$ as expected. However, for positive and negative values of $\gamma(b-a)$, the distribution slants towards $s=1$ and $s=-1$, respectively. The magnitude of the minimum becomes smaller as the value of $\gamma(b-a)$ gets larger.

Mode II stress intensity factor quantifies the strength of singularity for the shear stress at the end points of the interfacial zone. In Table 1, we provide the dimensionless SIFs, $K_{IIn}(a)$ and $K_{IIn}(b)$, as functions of $\gamma(b-a)$. The signs of the shear stress at the end points imply that $K_{IIn}(a)$ is positive and $K_{IIn}(b)$ is negative. The results provided in Table 1 are in agreement with this outcome. Additionally, magnitude of $K_{IIn}(a)$ decreases and that of $K_{IIn}(b)$ increases with the corresponding increase in the inhomogeneity parameter, $\gamma(b-a)$.

Since the half-plane is laterally graded, the location of the piezoelectric thin film also has a bearing on the response under electric field loading. In problems involving a homogeneous surface or a half-plane graded in the thickness direction, thin film location does not impart any influence since the problem is self-similar with respect to thin film translation. However, for a laterally graded half-plane,

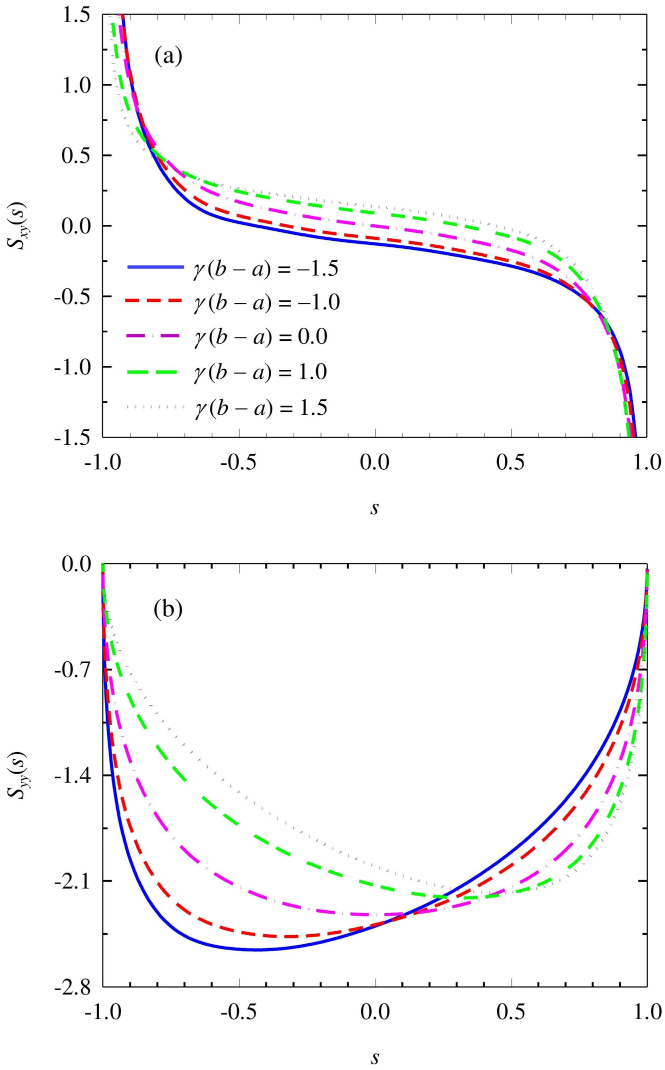

FIG. 10. Dimensionless interfacial shear and thin film normal stress as functions of $\gamma(b-a)$: (a) dimensionless shear stress; (b) dimensionless normal stress; $b = -a/2$, $\mu_0/E_f = 0.3$, $(b-a)/h = 10$, $\nu = 0.25$.

the shear modulus varies in the lateral direction, and thus a shift in the location of the thin film causes variations in stress distributions. Figure 11 presents, dimensionless shear stress, $S_{xy}(s)$, and dimensionless thin film stress, $S_{yy}(s)$, for five different thin film locations. The inhomogeneity parameter, $\gamma(b-a)$, is assumed to be equal to 1. The impact of punch location is seen to be particularly significant on the thin film stress. As the position of the thin film shifts in the

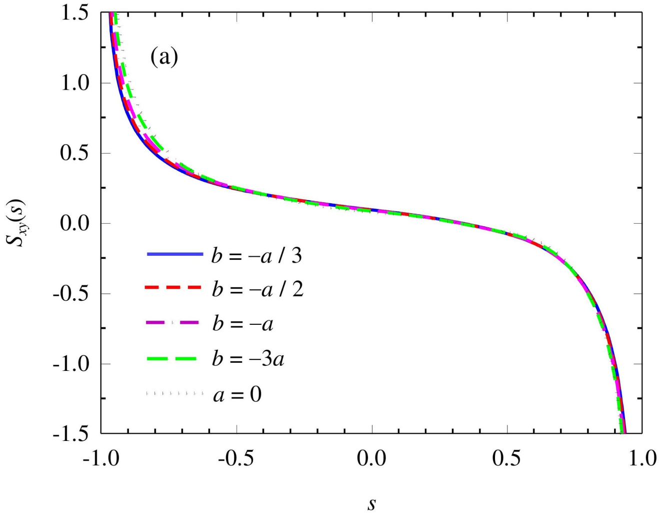

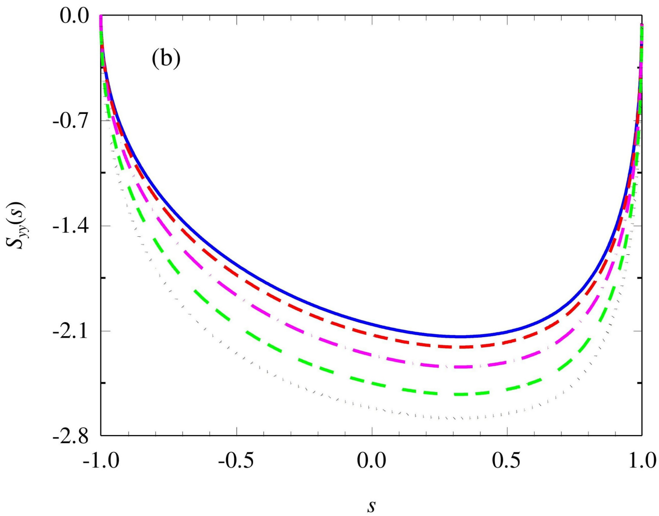

Fig. 11. Dimensionless interfacial shear and thin film normal stress as functions of thin film location: (a) dimensionless shear stress, (b) dimensionless normal stress; $\gamma(b-a)=1$, $\mu_0/E_f=0.3$, $(b-a)/h=10$, $\nu=0.25$.

positive y-direction from the configuration $b=-a/3$ to $a=0$, magnitude of the compressive thin film stress increases. Table 2 shows the dimensionless mode II stress intensity factors for five different configurations. As the thin film translates in the y-direction, $K_{IIn}(a)$ becomes larger and $K_{IIn}(b)$ decreases.

Figure 12 examines the effect of the thin film length-to-thickness ratio, $(b-a)/h$, on the stress components. Dimensionless shear stresses given in

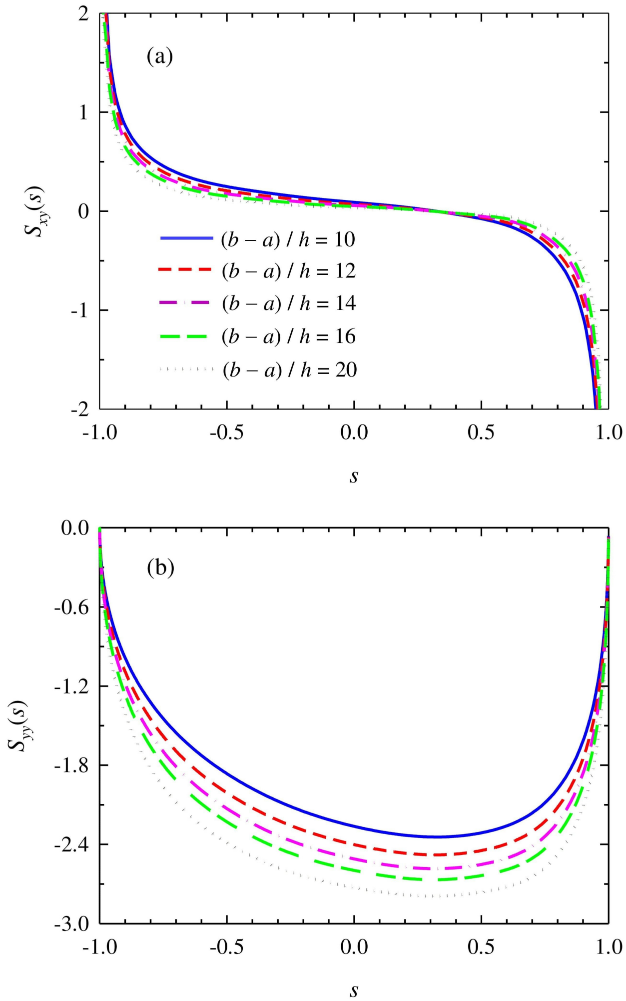

FIG. 12. Dimensionless interfacial shear and thin film normal stress as functions of length-to-thickness ratio: (a) dimensionless shear stress; (b) dimensionless normal stress; $b = -a$, $\gamma(b - a) = 1$, $\mu_0/E_f = 0.3$, $\nu = 0.25$.

TABLE 1. Mode II stress intensity factors at the end points of the interface; $b = -a/2$, $\mu_0/E_f = 0.3$, $(b - a)/h = 10$, $\nu = 0.25$.

	$\gamma(b-a)$				
	-1.5	-1.0	0.0	1.0	1.5
$K_{IIn}(a)$	0.8455	0.7051	0.4775	0.3028	0.2354
$K_{IIn}(b)$	-0.3294	-0.3758	-0.4775	-0.5807	-0.6352

TABLE 2. Mode II stress intensity factors at the end points of the interface; $\gamma(b-a)=1$, $\mu_0/E_f=0.3$, $(b-a)/h=10$, $\nu=0.25$.

	$b=-a/3$	$b=-a/2$	$b=-a$	$b=-3a$	$a=0$
$K_{IIn}(a)$	0.2864	0.3028	0.3378	0.3960	0.4614
$K_{IIn}(b)$	−0.5521	−0.5807	−0.6409	−0.7388	−0.8467

Fig. 12(a) become zero in the interval $(0.3, 0.33)$, and the intercepts are close to each other. At either side of the intercept, an increase in $(b-a)/h$ causes a reduction in the magnitude of the dimensionless shear stress. This trend is seen to be reversed for the dimensionless thin film normal stress, $S_{yy}(s)$, i.e., the larger length-to-thickness ratio amplifies the stress magnitude. Table 3 tabulates the mode II SIFs as functions of the length-to-thickness ratio. $K_{IIn}(a)$ and $K_{IIn}(b)$ are respectively, decreasing and increasing functions of $(b-a)/h$.

TABLE 3. Mode II stress intensity factors at the end points of the interface; $b=-a$, $\gamma(b-a)=1$, $\mu_0/E_f=0.3$, $\nu=0.25$.

	$(b-a)/h$				
	10	12	14	16	20
$K_{IIn}(a)$	0.3378	0.3163	0.2984	0.2832	0.2587
$K_{IIn}(b)$	−0.6409	−0.5928	−0.5535	−0.5207	−0.4687

Elasticity of the piezoelectric thin film is another factor to be considered in the stress analysis. Figure 13 depicts the influence of μ_0/E_f, where μ_0 is the shear modulus of the half-plane surface; and E_f is effective Young's modulus of the piezoelectric thin film. The dimensionless inhomogeneity parameter, $\gamma(b-a)$, is taken as 1.0 and $b=-a$; thus, there are shifts in the s − intercepts of the shear stress curves and they are not perfectly symmetric with respect to $s=0$. The increase in μ_0/E_f causes decreases in S_{xy} magnitudes on both sides of the intercepts. The influence on the thin film normal stress is also notable. The magnitude of the normalized normal stress becomes smaller with the increase in the ratio, μ_0/E_f. The results regarding the mode II SIFs are tabulated in Table 4. The increase in μ_0/E_f causes corresponding drops in SIF magnitudes at both corners.

TABLE 4. Mode II stress intensity factors at the end points of the interface; $b=-a$, $\gamma(b-a)=1$, $(b-a)/h=10$, $\nu=0.25$.

	μ_0/E_f				
	0.1	0.2	0.3	0.4	0.5
$K_{IIn}(a)$	0.4637	0.3862	0.3378	0.3040	0.2787
$K_{IIn}(b)$	−0.9364	−0.7518	−0.6409	−0.5658	−0.5109

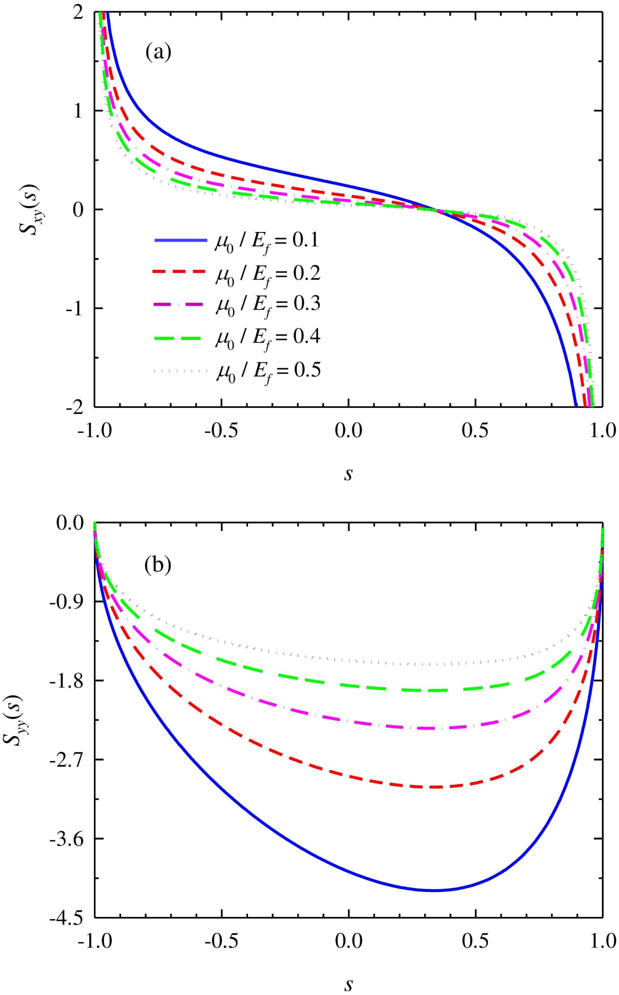

Fig. 13. Dimensionless interfacial shear and thin film normal stress as functions of μ_0/E_f: (a) dimensionless shear stress; (b) dimensionless normal stress; $b = -a$, $\gamma(b-a) = 1$, $(b-a)/h = 10$, $\nu = 0.25$.

Contour plots of normalized displacement in the y-direction and the shear stress generated by the finite element method are provided in Fig. 14. Normalized forms are defined by

$$\bar{u}_y = \frac{u_y}{h\frac{e_f}{E_f}E_x^{(\mathrm{f})}}, \qquad \bar{\sigma}_{xy} = \frac{\sigma_{xy}}{\mu_0\frac{e_f}{E_f}E_x^{(\mathrm{f})}}. \tag{4.1}$$

The two-dimensional distributions are obtained for 5 different values of the ratio, μ_0/E_f. They illustrate stress intensifications and relatively larger displacements at the end points of the interfacial zone and the thin film, respectively.

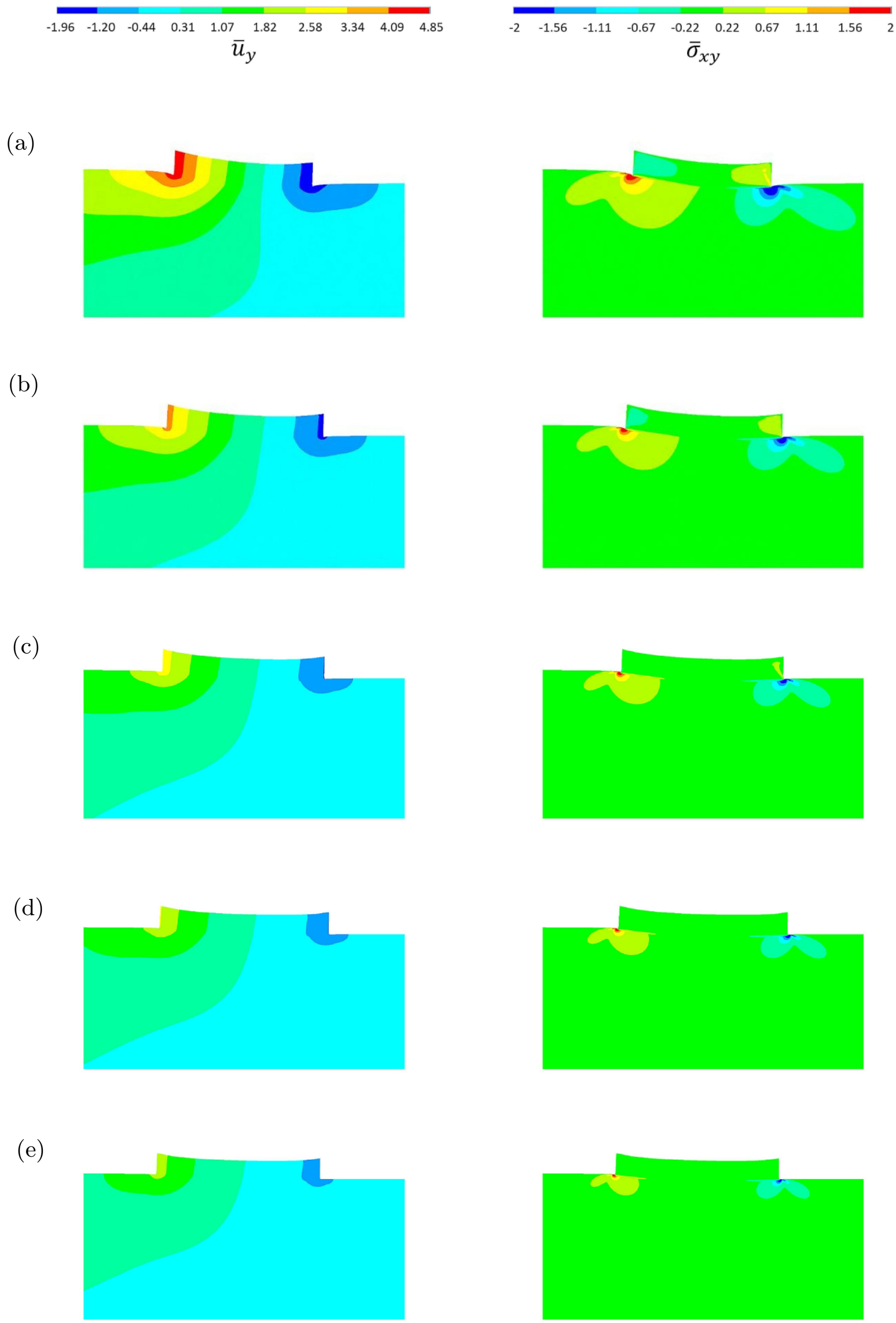

Fig. 14. Normalized horizontal displacement (left column) and shear stress (right column) contours generated by FEM: (a) $\mu_0/E_f = 0.1$, (b) $\mu_0/E_f = 0.2$, (c) $\mu_0/E_f = 0.3$, (d) $\mu_0/E_f = 0.4$, (e) $\mu_0/E_f = 0.5$; $b = -a$, $\gamma(b-a) = 1.0$, $(b-a)/h = 10$, $\nu = 0.25$.

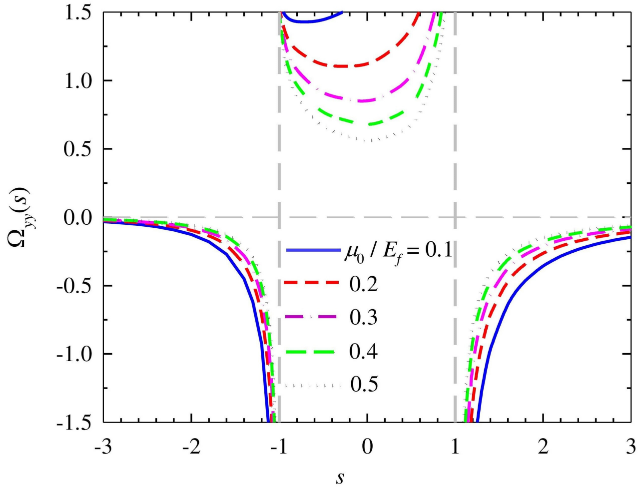

Fig. 15. Dimensionless lateral stress, $\Omega_{yy}(s)$, for five different values of μ_0/E_f; $\gamma(b-a) = 1.0$, $b = -a$, $\nu = 0.25$.

Variations of the dimensionless normal stress in the lateral direction at the surface of the graded half-plane, $\Omega_{yy}(s)$, are presented in Figs. 15 and 16. The numerical results shown in both figures are generated by means of the analytical technique. Figure 15 depicts $\Omega_{yy}(s)$ distributions for five different values of the modulus ratio, μ_0/E_f. The impact of μ_0/E_f is seen to be significant. Both inside ($|s| < 1$) and outside ($|s| > 1$) of the interfacial region, the magnitude of the

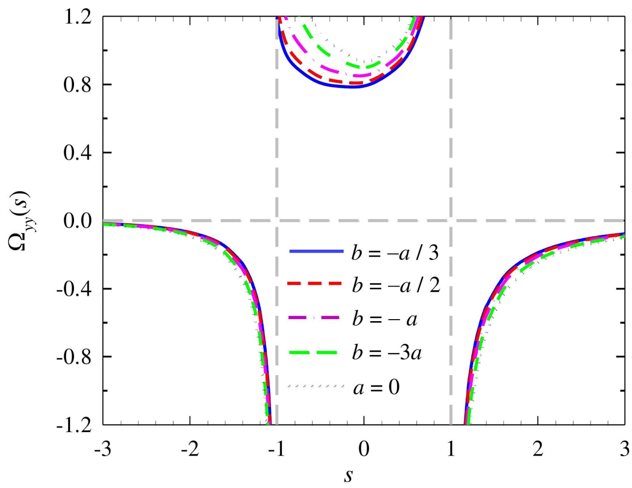

Fig. 16. Dimensionless lateral stress, $\Omega_{yy}(s)$, for five different positions of the piezoelectric thin film; $\gamma(b-a) = 1.0$, $\mu_0/E_f = 0.3$, $\nu = 0.25$.

dimensionless stress lessens as μ_0/E_f is increased from 0.1 to 0.5. The normal stress possesses positive singularities at the end points of the interfacial region, which are thus deemed to be critical locations for the crack initiation and growth. Figure 16 examines the influence of the location of the piezoelectric thin film on the lateral normal stress distribution. The effect is particularly noticeable within the interface. The normal stress in this zone becomes larger as b value is varied from $-a/3$ to $-3a$; and the largest magnitude is calculated for $a = 0$. Note that the thin film is at the leftmost location for $b = -a/3$ and the rightmost location for $a = 0$.

5. Conclusions

Analytical and computational methods are developed to calculate stresses in an advanced material system, consisting of a piezoelectric thin film and a laterally graded half-plane. The external loading is assumed to be a uniform electric field applied to the thin film across the thickness direction. Two separate verification studies are carried out to assess the levels of accuracy associated with the analytical and computational procedures. In the first set of computations, the analytical results are compared to those calculated by means of the finite element method. The second study involves a comparison to the stress distribution for a limiting case available in the literature. In both studies, a very good agreement is observed, which is indicative of the high level of accuracy achieved in the implementations of the analytical and computational procedures.

The developed analytical technique is capable of accounting for a number of parameters including, dimensionless inhomogeneity parameter, $\gamma(b-a)$; thin film location parameter, b/a; modulus ratio, μ_0/E_f; and thin film length-to-thickness ratio, $(b-a)/h$. Parametric analyses indicate that the impact of each of these parameters on stress distributions is significant. The increase in the inhomogeneity parameter, $\gamma(b-a)$, is found to cause a positive shift in the shear stress magnitude within the inner section of the interfacial zone. Thin film normal stress goes through a minimum and the location of the extremum point translates in the positive s-direction as $\gamma(b-a)$ is increased from -1.5 to 1.5. An increase in either μ_0/E_f or $(b-a)/h$ results in a corresponding rise in the magnitude of the normal stress within the thin film.

The stress intensity factor is the primary parameter that represents the strength of a singular field. In the present study, we defined the mode II SIFs at the end points by considering the shear stress at the interface of the piezoelectric thin film and the laterally graded half-plane. The inhomogeneity parameter, $\gamma(b-a)$, possesses a particularly significant influence on the dimensionless SIFs, $K_{IIn}(a)$ and $K_{IIn}(b)$. It is found that as $\gamma(b-a)$ is increased from -1.5 to 1.5, the magnitude of $K_{IIn}(a)$ drops 72.2% whereas that of $K_{IIn}(b)$ increases 92.8%.

Another important factor that affects fracture mechanisms in piezoelectric thin film-substrate systems is the normal stress in the lateral direction at the surface of the substrate. Our numerical results identify positive singularities in the lateral normal stress at the end points of the interface, which could thus be potential sites for impending crack propagation. An increase in the modulus ratio, μ_0/E_f, causes a reduction in the lateral normal stress magnitude within the central zone of the interface. The thin film location also affects the normal stress in this region. For the considered parameters, the highest magnitude is generated when the thin film is at the rightmost location.

Structural integrity and failure analyses involving piezoelectric thin films and laterally graded surfaces require reliable estimations of strains, stresses, and SIFs. These quantities can then be utilized in conjunction with appropriate failure theories or fracture criteria to assess the electro-mechanical behavior of the system components. The dual approach methodology presented in this article allows determination of singularities, stress components and stress intensity factors as functions of the parameters that describe inhomogeneity, geometry, and elasticity. The methods proposed could therefore prove useful in analysis, design, and optimization studies of advanced material systems that comprise piezoelectric and graded components.

References

1. J. Jitcharoen, N.P. Padture, A.E. Giannakopoulos, S. Suresh, *Hertzian-crack suppression in ceramics with elastic-modulus-graded surfaces*, Journal of the American Ceramic Society, **81**, 2301–2308, 1998.

2. Y. Zhoy, Q. Lin, J. Hong, N. Yang, *Optimal design of functionally graded material for stress concentration reduction*, Structures, **29**, 561–569, 2021.

3. Z.-H. Jin, R.C. Batra, *Stress intensity relaxation at the tip of an edge crack in functionally graded material subjected to a thermal shock*, Journal of Thermal Stresses, **19**, 317–339, 1996.

4. B.L. Wang, N. Noda, *Design of a smart functionally graded thermopiezoelectric composite structure*, Smart Materials and Structures, **10**, 189–193, 2001.

5. J. Cheng, B. Sun, M. Wang, Z. Li, *Analysis of III crack in a finite plate of functionally graded piezoelectric/piezomagnetic materials using boundary collocation method*, Archive of Applied Mechanics, **89**, 231–243, 2018.

6. P.G. Lashmi, P.V. Ananthapadmanabhan, G. Unnikrishnan, S.T. Aruna, *Present status and future prospects of plasma sprayed multilayered thermal barrier coating systems*, Journal of the European Ceramic Society, **40**, 2731–2745, 2020.

7. S. Kaushal, D. Gupta, H. Bhowmick, *Wear behavior of microwave-processed Ni-WC8Co-based functionally graded materials*, Proceedings of the Institution of Mechanical Engineers, Part L: Journal of Materials: Design and Applications, **235**, 5, 1036–1045, 2021.

8. L. Wang, J. Zhang, Z. Zeng, Y. Lin, L. Hu, Q. Xue, *Fabrication of a nanocrystalline Ni-Co/CoO functionally graded layer with excellent electrochemical corrosion and tribological performance*, Nanotechnology, **17**, 4614–4623, 2006.

9. H. Niknam, A.H. Akbarzadeh, *Graded lattice structures: simultaneous enhancement in stiffness and energy absorption*, Materials & Design, **196**, 109129, 2020.

10. S. Vijayavenkataraman, L.Y. Kuan, W.F. Lu, *3D-printed ceramic triply periodic minimal surface structures for design of functionally graded bone implants*, Materials & Design, **191**, 108602, 2020.

11. W. Zhou, R.-C. Wang, C.-Q. Peng, Z.-Y. Cai, *Microstructure and properties of Al-Si functionally graded materials for electronic packaging*, Transactions of Nonferrous Metals Society of China, **33**, 3583–3596, 2023.

12. I. Eshraghi, S. Dag, *Transient dynamic analysis of functionally graded micro-beams considering small-scale effects*, Archives of Mechanics, **73**, 303–337, 2021.

13. F.Y. Genao, J. Kim, K.K. Zur, *Nonlinear finite element analysis of temperature-dependent functionally graded porous micro-plates under thermal and mechanical loads*, Composite Structures, **256**, 112931, 2021.

14. W. Meng, X. Yin, W. Zhang, J. Fang, L. Guo, Q. Ma, B. Cui, *Additive manufacturing of a functionally graded material from Inconel625 to Ti6Al4V by laser synchronous preheating*, Journal of Materials Processing Technology, **275**, 116368, 2020.

15. L. Yan, Y. Chen, F. Liou, *Additive manufacturing of functionally graded metallic materials using laser metal deposition*, Additive Manufacturing, **31**, 100901, 2020.

16. M. Ansari, E. Jabari, E. Toyserkani, *Opportunities and challenges in additive manufacturing of functionally graded metallic materials via powder-fed laser directed energy deposition: a review*, Journal of Materials Processing Technology, **294**, 117117, 2021.

17. J. Zhang, C. Li, L. Ba, X. Di, *Transition strategy optimization of Inconel625-HSLA steel functionally graded material fabricated by wire arc additive manufacturing*, Metals and Materials International, **29**, 767–776, 2023.

18. Y. Alinia, M. Espo, *Sliding contact problem of an FGM coating/substrate system with two-dimensional material property grading*, Acta Mechanica, **231**, 649–659, 2020.

19. O. Arslan, *Hertz-type frictional contact problem of a bidirectionally graded half-plane indented by a sliding rounded punch*, Mechanics of Materials, **149**, 103539, 2020.

20. S. Dag, M.A. Guler, B. Yildirim, A.C. Ozatag, *Sliding frictional contact between a rigid punch and a laterally graded elastic medium*, International Journal of Solids and Structures, **46**, 4038–4053, 2009.

21. M.A. Attia A.G. El-Shafei, *Investigation of multibody receding frictional indentation problems of unbonded elastic functionally graded layers*, International Journal of Mechanical Sciences, **184**, 105838, 2020.

22. R. Cao, C. Mi, *On the receding contact between a graded and a homogeneous layer due to a flat-ended indenter*, Mathematics and Mechanics of Solids, **27**, 775–793, 2022.

23. E. Öner, B.T. Tabano, E.U. Yaylaci, G. Adiyaman, M. Yaylaci, A. Býrýncý, *On the plane receding contact between two functionally graded layers using computational, finite element and artificial neural network methods*, Zeitschrift für Angewandte Mathematik und Mechanik, **102**, e202100287, 2022.

24. P. Fu, J. Zhao, X. Zhang, H. Miao, Z. Wen, P. Wang, Q. Kan, G. Kang, *Modeling of fully coupled thermo-elastic sliding contact of coated systems*, International Journal of Heat and Mass Transfer, **223**, 125213, 2024.

25. J. Liu, L.-L. Ke, Y.-S. Wang, *Two-dimensional thermoelastic contact problem of functionally graded materials involving frictional heating*, International Journal of Solids and Structures, **48**, 2536–2548, 2011.

26. A. Talezadehlari, A. Nikbakht, M. Sadighi, A. Zucchelli, *Numerical analysis of frictional contact in the presence of a surface crack in a functionally graded coating substrate system*, International Journal of Mechanical Sciences, **117**, 286–298, 2016.

27. I. Çömez, *Frictional moving contact problem between a conducting rigid cylindrical punch and a functionally graded piezoelectric layered half plane*, Meccanica, **56**, 3039–3058, 2021.

28. Y. Wang, X. Zhang, L.M. Keer, H. Shen, *Sub-Rayleigh elastodynamic frictional contact of a layer-substrate system*, Tribology International, **148**, 106299, 2020.

29. E. Fortunato, P. Barquinha, R. Martins, *Oxide semiconductor thin-film transistors: a review of recent advances*, Advanced Materials, **24**, 2945–2986, 2012.

30. T.D. Lee, A.U. Ebong, *A review of thin film solar cell technologies and challenges*, Renewable and Sustainable Energy Reviews, **70**, 1286–1297, 2017.

31. X. Song, Y. Lu, F. Wang, X. Zhao, H. Chen, *A coupled electro-chemo-mechanical model for all-solid-state thin film Li-ion batteries: the effects of bending on battery performances*, Journal of Power Sources, **452**, 227803, 2020.

32. R. Thomas, J.F. Scott, D.N. Bose, R.S. Katiyar, *Multiferroic thin-film integration onto semi conductor devices*, Journal of Physics: Condensed Matter, **22**, 423201, 2010.

33. V.V. Anusha Thampi, A. Bendavid, B. Subramanian, *Nanostructured TiCrN thin films by pulsed magnetron sputtering for cutting tool applications*, Ceramics International, **42**, 9940–9948, 2016.

34. J.-M. Liu, B. Pan, H.L.W. Chan, S.N. Zhu, Y.Y. Zhu, Z.G. Liu, *Piezoelectric coefficient measurement of piezoelectric thin films: an overview*, Materials Chemistry and Physics, **75**, 12–18, 2002.

35. K. Tao, H. Yi, L. Tang, J. Wu, P. Wang, N. Wang, L. Hu, Y. Fu, J. Miao, H. Chang, *Piezoelectric ZnO thin films for 2DOF MEMS vibrational energy harvesting*, Surface and Coatings Technology, **359**, 289–295, 2019.

36. M.A. Guler, *Mechanical modeling of thin films and cover plates bonded to graded substrates*, Journal of Applied Mechanics-Transactions of the ASME, **75**, 051105-1, 2008.

37. M.A. Guler, Y.F. Gülver, E. Nart, *Contact analysis of thin films bonded to graded coatings*, International Journal of Mechanical Sciences, **55**, 50–64, 2012.

38. P. Chen, S. Chen, J. Peng, *Interface behavior of a thin-film bonded to a graded layer coated elastic half-plane*, International Journal of Mechanical Sciences, **115–116**, 489–500, 2016.

39. P. Chen, J. Peng, L. Yu, Y. Yang, *The interfacial analysis of a film bonded to a finite thickness graded substrate*, International Journal of Solids and Structures, **120**, 57–66, 2017.

40. C. Peijian, C. Shaohua, G. Wang, G. Feng, *The interface behavior of a thin piezoelectric film bonded to a graded substrate*, Mechanics of Materials, **127**, 26–38, 2018.

41. D. Li, P. Chen, Z. Huang, H. Liu, S. Chen, *The interfacial behavior of a thermoelectric thin-film bonded to an orthotropic substrate*, International Journal of Solids and Structures, **267**, 112160, 2023.

42. Y. Liu, B.L. Wang, C. Zhang, *Mechanical model for a thermoelectric thin film bonded to an elastic infinite substrate*, Mechanics of Materials, **114**, 88–96, 2017.

43. F.O. Falope, L. Lanzoni, E. Radi, A.M. Tarantino, *Thin film bonded to elastic orthotropic substrate under thermal loading*, The Journal of Strain Analysis for Engineering Design, **51**, 256–269, 2016.

44. E. Nart, Y. Alinia, M.A. Güler, *The effect of material anisotropy on the mechanics of a thin-film/substrate system under mechanical and thermal loads*, Mathematics and Mechanics of Solids, **27**, 644–661, 2022.

45. H.S. Hedia, N. Fouda, *Design optimization of cementless hip prosthesis coating through functionally graded material*, Computational Materials Science, **97**, 83–87, 2014.

46. A.O. Ghaziani, R. Soheilifard, S. Kawsar, *The effect of functionally graded materials on bone remodelling around osseointegrated trans-femoral prostheses*, Journal of the Mechanical Behavior of Biomedical Materials, **118**, 104426, 2021.

47. S. Kumar, A. Mitra, H. Roy, *Forced vibration response of axially functionally graded non-uniform plates considering geometric nonlinearity*, International Journal of Mechanical Sciences, **128–129**, 194–205, 2017.

48. M. Mohammadnejad, *Free vibration analysis of axially functionally graded beams using Fredholm integral equations*, Archive of Applied Mechanics, **93**, 961–976, 2023.

49. S.E. Toktaş, S. Dag, *Mechanics of moving contacts involving functionally graded multiferroics*, Archives of Mechanics, **75**, 431–468, 2023.

50. F. Delale, F. Erdogan, *The crack problem for a half plane stiffened by elastic cover plate*, International Journal of Solids and Structures, **18**, 381–395, 1982.

51. Y. Chen, F. Erdogan, *The interface crack problem in nonhomogeneous bonded materials of finite thickness*, Final Project Report, Office of Naval Research Contract No. N00014-89-3188, Lehigh University, Bethlehem PA, USA, 1992.

52. I.M. Smith, D.V. Griffiths, L. Margetts, *Programming the Finite Element Method*, John Wiley & Sons, 2014.

53. S. Dag, B. Yildirim, F. Erdogan, *Interface crack problems in graded orthotropic media: Analytical and computational approaches*, International Journal of Fracture, **130**, 471–496, 2004.

54. B. Yildirim, S. Dag, F. Erdogan, *Three dimensional fracture analysis of FGM coatings under thermomechanical loading*, International Journal of Fracture, **132**, 369–395, 2005.

Received October 12, 2024; revised version January 13, 2025.
Published online April 2, 2025.